Analysis of the Angle Modulated Switching Strategy for use With Fractional Horse Power BLDC Motors

Felix Krall, *Graduate Student Member, IEEE*, Hannes Gruebler, and Annette Muetze, *Fellow, IEEE*

***Abstract*—In recent years, electromagnetic compatibility (EMC) has become progressively important because of the rise in the number of electronic auxiliary devices in motor vehicles. This article presents an angle modulated switching strategy for fractional horsepower drives. It allows decreasing the size of the necessary EMC filter, for the example case drive used, down to less than 50%, from nine to four capacitors. Simultaneously, it reduces the radiated electromagnetic emissions over a wide frequency range by almost 10 $\mathrm{dB}_{\mu\mathrm{V/m}}$. The EMC measurements performed in a shielded chamber are compared with the results for two conventional switching strategies. Subsequently, the influence of the presented switching strategy on the efficiency and on the emitted airborne and structure-borne noise is investigated.**

***Index Terms*—Brush less drive, electromagnetic compatibility (EMC)/electromagnetic interference (EMI), noise, pulsewidth modulation (PWM), switching strategy.**

I. INTRODUCTION

THE number of safety and comfort relevant systems is ever-increasing in the automotive sector. Additionally, more and more conventional drive concepts are being replaced by electric drives, e.g., electric oil and water pumps [1], [2], electric brake boosters [3], and super chargers [4]. Both trends increase the number of electric drives being installed. For example, numbers are determined using the Volkswagen (VW) Golf7: One VW Golf7 is equipped with 47 rotatory electric drives in the standard configuration [5]. Assuming that all 9 68 284 Golf7s manufactured in 2017 and all 805752 Golf7s manufactured in 2018 [6] were delivered in the standard configuration. This results in a total of approximately 45 million electric drives being installed in 2017 in VW Golf7s, and approximately 37 million in 2018. While these numbers are only for one specific model, they should convey the impressive volume of auxiliary drives currently used throughout the automotive sector.

Increasing requirements on the efficiency and the controllability of these drives has led to the use of brush less direct current (BLDC) motors, because they are known for their low maintenance, high power density, and high efficiency [7]. Every one of these drives is a possible source of electromagnetic emissions (EME).

Different techniques have been proposed to reduce the EME so as to comply to the limits according to the standard CISPR 25 [8]; hardware- and software-based approaches are distinguished. The first include measures such as shielding of the cable harness and/or the whole application, the filter design, the use of specific materials and components for the electromagnetic compatibility (EMC) filter, as well as the design of the printed circuit board (PCB). Details on these methods are provided in the respective literature (e.g., [9]–[12]). Such hardware-based approaches typically increase the costs for the overall system, and thus they are not suitable for low-cost mass products, as it is in the focus here. In contrast, software-based approaches to reduce the EME are very popular for low-cost applications, because they decrease the EME by use of the already available hardware of the drive.

While pulsewidth modulation (PWM) has been widely established to control the average current flow and thus power flow of voltage source supplied electric loads, its high switching frequency inherently comes with EME, which increases with switching frequency [13]. PWM-related EMC has been a subject of research for a long time. As a matter of fact, several different forms of PWM have been proposed to reduce EME and meet EMC regulations, thereby following a software-based approach. For example, spread-spectrum PWM, in which the switching frequency is not constant, spreads the switching frequency's energy and its harmonics. Thereby, the energy of the EME is spread over a wider range in the frequency domain; and thus, the single peaks are reduced. A simple variant, the frequency hopping PWM (FHPWM), operates at n different frequencies to reduce the EME [14]. With increasing computational power and decreasing cost, increasingly powerful spread-spectrum techniques are used, ranging from periodic [15] through random [16] to chaotic modulation [17] of the switching frequency. Comprehensive overviews of the different spread-spectrum techniques are given in [18] and [19]. For the sake of completeness, it should be mentioned that the spread-spectrum approach also positively affects the acoustic noise [20].

This article proposes an angle modulated switching strategy (AMSS), i.e., a different software-based approach, which allows reducing the switching frequency down to the electrical frequency. The six-step mode has been used for operating AC machines at their electrical frequency for decades, is well established, and has recently found a newed attention, e.g., [21], [22].

Manuscript received April 27, 2020; revised August 12, 2020; accepted September 17, 2020. Date of publication October 6, 2020; date of current version January 22, 2021. This work was supported in part by the Austrian Federal Ministry for Digital and Economic Affairs and in part by the National Foundation for Research, Technology, and Development. This paper was presented at the 21st European Conference on Power Electronics and Applications, Genova, Italy, September 2019. Recommended for publication by Associate Editor U. Deshpande. *(Corresponding author: Felix Krall.)*

The authors are with the Christian Doppler Laboratory for Brushless Drives for Pump and Fan Applications, Graz 8010, Austria, and also with the Electric Drives and Machines Institute, Graz University of Technology, Graz 8010, Austria (e-mail: felix.krall@tugraz.at; hannes.gruebler@tugraz.at; muetze@tugraz.at).

Color versions of one or more of the figures in this article are available online at https://ieeexplore.ieee.org.

Digital Object Identifier 10.1109/TPEL.2020.3028604

The proposed AMSS fundamentally differs from the six-step mode by its principle of operation: It controls the mean value of the voltage of the driven DC machine by adjusting the turn-ON and turn-OFF angles. This, in turn, determines the speed of the BLDC machine and not the base frequency, as in the case of AC machines. Therefore, the expected radiated EME are decreased. This in turn allows for a reduction of the EMC filter. For the example case drive, which is used as a cooling fan in an LED headlight, the required EMC filter was reduced from nine to four capacitors. This not only reduces the costs, but also increases the reliability of the electronics.

Because of the ever-increasing electrification of the automotive sector and modern combustion engines, the noise level, which previously masked disturbing noise, now decreases. Therefore, the demand for auxiliary systems with better noise performance is increasing [23]. While the proposed switching strategy increases the torque ripple, investigations on the noise have shown that the emitted noise does not increase significantly.

Selected results on the influence of the proposed switching strategy on the EMC performance have been presented in [24]. This article extends these results by extensive additional investigations of the EMC, measured at different speeds. Furthermore, the influences of the switching strategy on both the energy conversion efficiency of the drive system and on the acoustic noise are investigated. Section II introduces the proposed AMSS. Section III briefly describes the example case drive used and reviews the two state-of-the-art modulation schemes used for comparison, i.e., the conventional PWM and the frequency hopping PWM. The influence of the switching strategies on the conducted and radiated emissions is investigated in Section IV, while the influence on the efficiency is reported in Section V, the influence on the airborne and structure-borne sound is explored in Section VI. A higher rated motor is investigated in Section VII. Finally, Section VIII concludes this article.

II. ANGLE MODULATED SWITCHING STRATEGY

According to Parseval's theorem and the Fourier representation of the gating signals, the energies of the fundamental and of each of the harmonics do not change when the switching frequency increases; furthermore, the individual amplitudes remain constant [25]. However, the limits demanded by the standard CISPR 25 [8] decrease with higher frequencies. Hence, a reduced switching frequency can help the device pass the EMC tests [26], [27]. So, the main objective of the AMSS is to reduce the switching frequency to its minimum, namely the electrical frequency, to decrease the radiated emissions.

In contrast to the well-established six-step mode used for three phase AC machines, the AMSS controls the mean value of the voltage $\overline{U}$ by adjusting the turn-ON and turn-OFF angles. This, in turn, determines the speed of the BLDC machine and not the base frequency, as in the case of AC machines. In the example case drive, the switching frequency of the single MOSFETs is reduced to approximately 167 Hz for a rated speed of 5000 rpm, which results in a frequency of approximately 333 Hz for the current blocks in the cable harness. $\overline{U}$ is adjusted by the conduction angle α of the respective switch during an electrical period. In contrast to a fixed switching period with a varying duty cycle, the conduction angle in this case is adjustable, resulting in a speed-dependent switching period. Therefore, the proposed switching strategy is called the "AMSS." The angle

$$\alpha = \frac{\overline{U}}{U_{\mathrm{DC}}} \cdot 180^{\circ} \tag{1}$$

is the conduction angle in electrical degrees required to obtain a given $\overline{U}$. To obtain the maximum torque per Ampere for a given trapezoidal back-electromotive force (EMF), the voltage is supplied symmetrically around 90°, or 270°, respectively, electrically, see Fig. 1(a); the current blocks are in the middle of the electrical half-period. The alignment of the blocks at these positions also reduces the sensitivity to a possible error in the rotor position.

Because the on time is longer than the winding's time constant $\tau = {}^{L}/_{R}$, the current amplitude will increase until either the switch is turned OFF again, see Fig. 1(b), or until the current reaches its final value. Therefore, the AMSS does not offer the possibility to control the current amplitude.

III. METHODOLOGY

The performance of the proposed switching strategy is investigated with respect to its EMC, its efficiency, and its airborne as well as structure-borne sound. For its comparison to the conventional switching strategies PWM and FHPWM are used, so as to reference the possible performance improvement and/or drawbacks with respect to its being state of art.

A. Example Case Drive

A four-pole single-phase outer rotor BLDC motor with a concentrated random bifilar winding and trapezoidal back-EMF, which drives a radial fan for an automotive cooling application is used as the example case drive. Therefore, the range of the input voltage U_{DC} is 8–16 V. To keep the cooling capacity constant over the entire input voltage range, the fan is speed-controlled. Thus, also the power in the air gap and the average value of the phase currents are constant. The power in the airgap is 0.8 W, which corresponds to a torque of 1.54 mN·m and an average value of the phase currents of $\overline{i}_{\mathrm{phase}} = 214$ mA at the nominal point of 5000 rpm. Fig. 2 shows the equivalent circuit of the electric machine, the driving electronics, and the conducted emissions test setup. It comprises the supply voltage U_{DC}, the line impedance stabilization networks LISNs, a diode D for reverse polarity protection, a DC-link capacitor C, and the MOSFETs S_{A} and S_{B}. The phases A and B of the BLDC motor are modeled by the resistors R_{Cu}, the stray and main inductances L_{σ} and L_{m}, and the voltage sources u_{EMF} for the back-EMF, the motor parameters are listed in Table I. The bifilar winding consists of two wires wound in parallel, but in inverse directions. Therefore, the two phases are inversely magnetically coupled; this coupling is denoted by the dashed lines between the main inductances and the two dots. A positive current in phase A produces the same field distribution as a negative current in phase B. As a result, the high-side MOSFETs of a conventional H-bridge for a monofilar wound single-phase motor can be eliminated. This reduces the costs for the electronics and simplifies it. However, it doubles the copper spent on the bifilar winding. As the additional expense for the copper is more than outweighed

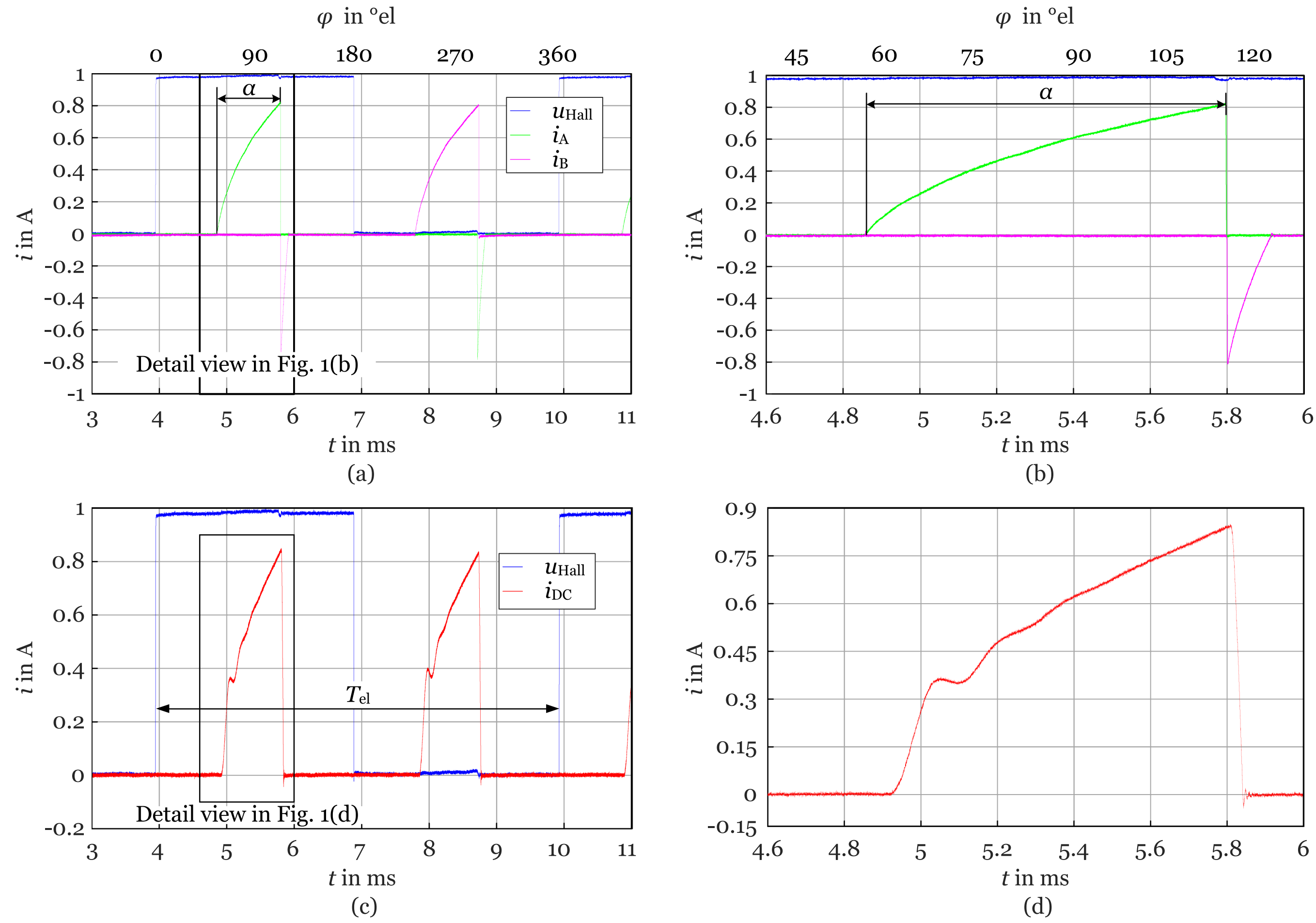

(a) (b) (c) (d)

Fig. 1. Measured currents for the AMSS: (a) Hall signal and phase currents; (b) Phase currents, detailed view; (c) Hall signal and cable harness current; (d) Cable harness current, detailed view; nominal operating point, $n = 5000$ rpm.

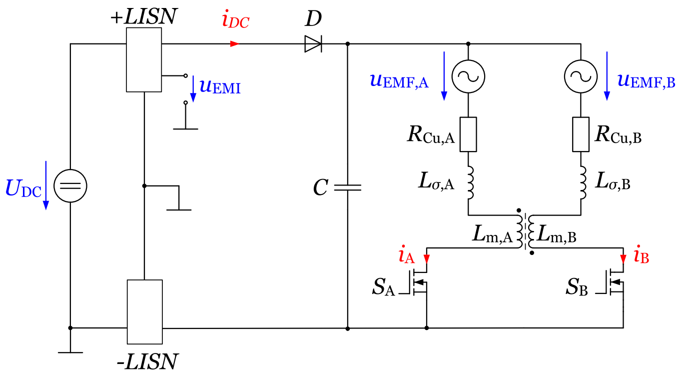

Fig. 2. Equivalent circuit of the conducted emissions test setup.

TABLE I
PARAMETERS OF THE EXAMPLE CASE DRIVE

Parameter	Value
U_{DC}	$8 - 16\,\text{V}$
R_{Cu}	$8.5\,\Omega$
L_{m}	$2.8\,\text{mH}$
L_{σ}	$260\,\mu\text{H}$
p	2

by the reduced cost for the electronics, the drive system with the bifilar winding is still more cost effective than the version with the unifilar winding.

B. Switching Strategies Investigated for Comparison

The proposed AMSS is compared to the conventional PWM and the FHPWM, both of which are state-of-the-art switching strategies. For comprehensiveness, these, including the nomenclature used, are briefly reviewed in the following:

1) Conventional PWM: PWM is a common method of controlling the average power of electrical loads. It switches with a fixed frequency (for the example case drive, $f_{\text{PWM}} = 20\,\text{kHz}$) between two states, the maximum and minimum of the voltage. The duty cycle d gives the fraction of one switching period in which the switch is active and can be determined by

$$d = \frac{\overline{U}}{U_{DC}} = \frac{T_{\text{ON}}}{T_{\text{PWM}}} = T_{\text{ON}} \cdot f_{\text{PWM}}. \tag{2}$$

The phase and the cable harness current for the conventional PWM with back-EMF zero-crossing commutation and advanced phase current turn-OFF to improve the performance [28] are shown in the Appendix, (see Figs. 16–19). During the ON-time of the switch, the current waveform is characterized by the winding's time constant $\tau = {}^{L}/_{R}$, the phase resistance, as well as the difference of the back-EMF u_{EMF} and the supply voltage U_{DC}. If the ON-time is much shorter than τ, as is the case with the PWM approaches, the stored magnetic energy in the inductance counteracts a change of the current amplitude. The current amplitude can thus be controlled by the PWM's duty cycle, as illustrated in the Appendix (see Figs. 13 and 17).

2) Frequency Hopping PWM: As opposed to the conventional PWM, which operates the switches at one fixed frequency, the FHPWM operates at n different frequencies to reduce the EME [14]. The choice of n and the switching frequencies is a tradeoff between effort and expected benefit (for the example, case drive, $n = 2$; $f_{\mathrm{PWM},1} = 22.89\,\mathrm{kHz}$, and $f_{\mathrm{PWM},2} = 34.33\,\mathrm{kHz}$). This results in n different PWM periods. Thus, all individual switching instances have different durations, although the duty cycle is the same for the whole electrical half-period

$$d = \frac{\overline{U}}{U_{\mathrm{DC}}} = \frac{T_{\mathrm{ON},1}}{T_{\mathrm{PWM},1}} = T_{\mathrm{ON},1} \cdot f_{\mathrm{PWM},1} = \frac{T_{\mathrm{ON},2}}{T_{\mathrm{PWM},2}} = T_{\mathrm{ON},2} \cdot f_{\mathrm{PWM},2}. \tag{3}$$

This is also illustrated in Fig. 13, shown in the Appendix along with the different durations of the phase current blocks influence the cable harness currents, in Fig. 15.

C. Systematic

Everyone of the three switching strategies to be investigated, is used to drive the MOSFETs to generate the desired average voltage $\overline{U}$ from the DC-link voltage. To eliminate any influence of effects other than the switching strategy on the results, all measurements were carried out on the same PCB layout.

IV. EMC ANALYSIS

A. Theory

Prior to market launch, a product has to pass an application specific EMC test. In one part of this test, the conducted and radiated emissions are measured. For the verification of the conducted emissions, the output voltage of the LISN u_{EMI} is measured; therefore, the cable harness current i_{DC} is decisive for this measurement. The influence of the frequency, the amplitude, and the duty cycle on the spectrum of a signal is described in [29]. Lower signal frequencies reduce high-order harmonics, a lower signal amplitude cuts down all the harmonics, and a reduced duty cycle decreases the low-order harmonics. Since the AMSS switches the corresponding MOSFET ON and OFF only once per electrical period, the current amplitude is a result of the circuit dynamics, but is not controlled itself. Therefore, the amplitude of the cable harness current for the AMSS is higher than for the PWM approaches. Fig. 1(c) illustrates such high current peaks, which may be compared to the currents of the conventional PWM or the FHPWM provided in the Appendix (see Figs. 14 and 18). However, the current does not contain any ripple, as is the case with the PWM approaches. The higher current amplitude and the absence of any high frequency current ripple leads to increased harmonics of the cable harness current in the frequency range up to approximately 500 kHz and reduced harmonics in the frequency range above.

To emit electromagnetic radiation into the environment, an antenna must be available, which must be excited by the appropriate frequencies. The frequency required for the excitation of the antenna is determined by its geometric dimensions. In general, however, antennas for higher frequencies can be smaller than for lower frequencies. Thus, a lower switching frequency helps to reduce the radiated emissions for the same antenna [26]. With respect to the bifilar wound fractional-horsepower application, the MOSFET is turned OFF, the phase current decreases to zero, and the second phase takes over the current flow. This is also illustrated by Fig. 1(b), as well as Figs. 13 and 17, provided in the Appendix. This results in steep edges in the full height of the phase current. In the case of the AMSS, due to the reduced switching frequency, this occurs only once within each phase per electrical period. Therefore, the harmonic content of the phase currents of the PWM approaches exceeds the harmonic content of the phase currents of the AMSS in the entire frequency range.

B. Measurement Setup

The measurement setup is based on the setup defined in the standard CISPR 25 [8]. Fig. 2 shows the equivalent circuit of the conducted emissions test setup. The two LISNs provide the standardized impedance to the input power of the device under test (DUT) and the measurement port for the conducted emissions measurement. The LISN's output voltage u_{EMI} is measured by the EMI receiver, assessed by the different detectors, and finally the resulting EMI spectrum is displayed [9]. For the measurement of the radiated emissions, the measurement setup is extended by a rod antenna, and the cable harness is adapted according to [8]. In this setup, the measured quantity is the output voltage of the antenna.

C. Measurement Results

The reduced switching frequency of the AMSS leads to a lower harmonic content of the phase currents and, hence, improves the EMC behavior when compared with the PWM approaches [26], [27]. This is illustrated in Fig. 3(a) and (b), which shows the conducted and radiated emissions for the different investigated switching strategies, measured at the nominal point of the example case drive. Fig. 3(a) shows the conducted emissions measurements using the quasi-peak detector. Although the conducted emissions of the AMSS in the low frequency range are slightly increased, the span to the limits still remains sufficient. Fig. 3(b) shows the measured radiated emissions, using the average detector. Due to the reduced number of capacitors, the FHPWM exceeds the limits and the PWM is very close to the limits, while the AMSS still decreases the radiated emissions by almost $10\,\mathrm{dB}_{\mu\mathrm{V/m}}$ over a wide frequency range, although the size of the EMC filter was reduced from nine to four capacitors.

Fig. 4 depicts the conducted and radiated emissions for the AMSS at different speeds and with the reduced EMC filter. Because the AMSS operates the single MOSFETs with the electrical frequency (166.66 Hz for 5000 rpm), at 150 kHz, the amplitudes

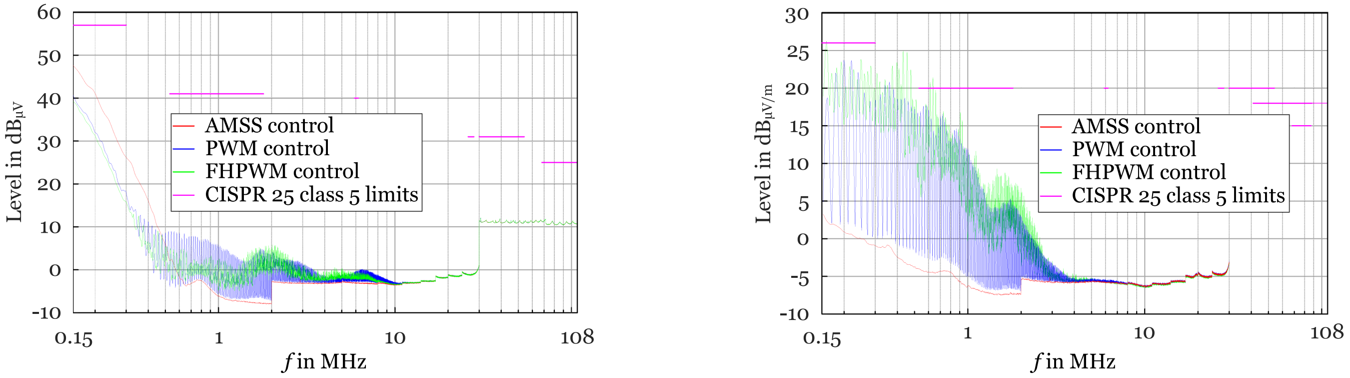

(a) (b)

Fig. 3. Measured EMC performance for the three investigated switching strategies, measured according to [8], with four instead of nine capacitors on the PCB, limits CIPSR 25 class 5: (a) conducted emissions, quasi peak detector, and (b) radiated emissions, average detector; nominal operating point, $n = 5000$ rpm.

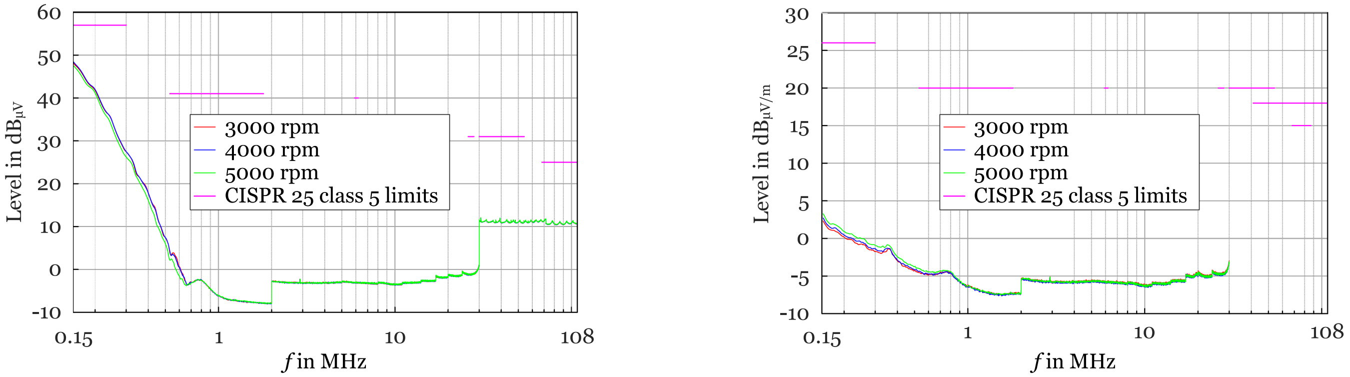

(a) (b)

Fig. 4. Measured EMC performance for the AMSS at different speeds and 13.5 V, measured according to [8], with four instead of nine capacitors on the PCB, limits CIPSR 25 class 5: (a) conducted emissions, quasi peak detector, and (b) radiated emissions, average detector.

of the single harmonics already decreased to an insignificant value. Thus, the measured emissions hardly change for a wide speed range.

For a reduced speed, the current drawn by the motor decreases. Independently of the speed, the PWM approaches operate the MOSFETs with the PWM frequencies. Due to the reduced current, the single harmonics for the PWM approaches decrease. However, because of the high switching frequencies, the single harmonics for the PWM switching strategies do not decrease as strongly as with the AMSS at 150 kHz. Thus, the emitted conducted and radiated EME decrease with lower speeds for the PWM approaches.

V. EFFICIENCY ANALYSIS

A. Theory

Due to the bifilar characteristic of the motor winding, the major part of the magnetic flux is coupled with both phases. Therefore, when phase A is switched OFF, phase B takes over the energy stored in the magnetic field

$$W_{\mathrm{mag},L_{\mathrm{m}}} = \frac{1}{2} L_{\mathrm{m,A}} \cdot i_{\mathrm{A}}^2 \tag{4}$$

and, thus, the corresponding current as well. This is illustrated in Fig. 1(b) in Section II, as well as in Figs. 13 and 17, provided in the Appendix.

The energy stored in the stray inductance

$$W_{\mathrm{mag},L_\sigma} = \frac{1}{2} L_{\sigma,\mathrm{A}} \cdot i_{\mathrm{A}}^2 \tag{5}$$

is only coupled with phase A, so phase B cannot take over the energy stored in the stray field of phase A, when phase A is switched OFF. Therefore, this energy is converted to heat in the MOSFET of phase A. The considerations above also apply for the change from phase B to phase A. These losses occur in the channels of the MOSFETs. Assuming that the parasitic MOSFET capacitances are lossless energy buffers, the drain to source losses represents the main part of the switching losses [30]. The average power loss in the channels of the MOSFETs P_{DS} is described by

$$P_{\mathrm{DS}} = \frac{1}{T_{\mathrm{el}}} \int_{T_{\mathrm{el}}} \left(u_{\mathrm{DS,A}} \cdot i_{\mathrm{A}} + u_{\mathrm{DS,B}} \cdot i_{\mathrm{B}} \right) dt \tag{6}$$

where T_{el} is the electrical period and u_{DS} is the drain to source voltage of the MOSFET. High values for u_{DS} and i only occur simultaneously during turn-ON and turn-OFF of the MOSFETs. Thus, a reduced switching frequency decreases the switching losses, i.e., $P_{\text{DS}} \propto f_{\text{sw}}$. For the same RL-element, a higher current results in an increased induced voltage at any given turn-OFF instant and, thus increased switching losses.

The ohmic losses in the bifilar winding of the motor are proportional to the square of the current and linearly dependent on the ON time, resulting in $P_{\text{DS}} \propto i^2$ and $P_{\text{DS}} \propto T_{\text{ON}}$. Due to (6), the ohmic losses in the MOSFETs are part of the drain to source losses, so the remaining ohmic losses in the winding can be written as

$$P_{\text{ohmic}} = \frac{1}{T_{\text{el}}} \int_{T_{\text{el}}} \left(R_{\text{Cu,A}} \cdot i_{\text{A}}^2 + R_{\text{Cu,B}} \cdot i_{\text{B}}^2 \right) dt. \tag{7}$$

Because the switching losses are proportional to the switching frequency, and the AMSS operates the MOSFETs at a significantly reduced frequency, the switching losses should decrease. Depending on the supply voltage U_{DC} and the circuit dynamics, the amplitude and the duration of the phase current blocks will adjust accordingly for the AMSS. Due to $P_{\text{ohmic}} \propto i^2$ and $P_{\text{ohmic}} \propto T_{\text{ON}}$, the ohmic losses decrease faster with a decreasing supply voltage for the AMSS than for the PWM approaches. Therefore, the overall losses should decrease faster for the AMSS than for the PWM approaches.

B. Measurement Setup

The different quantities were measured using 120 MHz differential probes with 1 % gain accuracy (u_{DS}, u_{EMF}, and u_{Hall}) and 100 MHz current probes also with 1 % accuracy (i_{DC} and i_{phase}), via a 2.5 GHz digital storage oscilloscope. The input power of the DUT (P_{DC}) was measured using a data recorder with a sample frequency of 2 MS/s and a basic accuracy of 0.02 %.

C. Measurement Results

For the following measurements, the same example case drive is operated under the same conditions (U_{DC} and n). Therefore, the difference in the losses and also in the consumed power is related to the switching strategy. Hereafter, the influence of the switching strategy and the supply voltage on the switching losses and the ohmic losses is investigated.

Although the phase current and, thus the drain to source voltage at turn-OFF of the MOSFETs increases, the switching losses are lower for the AMSS than for the PWM approaches. This is due to the drastically reduced switching frequency. The AMSS reduces the switching losses in the nominal point from 90 down to 8 mW.

The switching period of the AMSS is longer than τ, thus the current shows exponential behavior [see Fig. 1(b)]. At the nominal operating point, the current amplitude of the AMSS is twice as high as for the PWM techniques. The ON-time of the AMSS is only about half of the FHPWM's ON-time. This is illustrated in Fig. 1(b) in Section II and Fig. 12, provided in the Appendix. As a result, the ohmic losses increase from 745 mW for the FHPWM to 931 mW for the AMSS.

For a reduced supply voltage U_{DC}, the difference between the back-EMF and the supply voltage decreases also. Therefore, the amplitude of the AMSS's current blocks is reduced. To maintain constant speed of the fan, the mean value of (10) must remain constant. So, if the amplitude of the current blocks decreases, the duration has to increase accordingly. Due to $P_{\text{ohmic}} \propto i^2$ and $P_{\text{ohmic}} \propto T_{\text{ON}}$, the ohmic losses for the AMSS decrease. In addition to the current, the voltage u_{DS}, which the MOSFET must absorb at power-ON and at power-OFF, also decreases. As a result, also the switching losses decrease.

TABLE II
POWER CONSUMPTION FOR THE INVESTIGATED SWITCHING STRATEGIES AT DIFFERENT SUPPLY VOLTAGE LEVELS AND A SPEED OF 5000 rpm

Power Consumption - 5000 rpm			
-	AMSS	FHPWM	PMW
U	P_{DC}	P_{DC}	P_{DC}
V	W	W	W
8.5	1.64	1.91	1.91
12.5	2.16	2.16	2.13
13.5	2.28	2.17	2.15
16.0	2.64	2.32	2.29

To maintain constant speed with the FHPWM for a reduced supply voltage, the duty cycle must increase. The PWM periods of the FHPWM are shorter than τ, thus the current amplitude hardly changes, as do the ohmic losses. The voltage of (6) decreases according to the reduction of the supply voltage U_{DC}, therefore, also the switching losses decrease. Since $P_{\text{DS}} \propto i \cdot u_{\text{DS}}$ and $P_{\text{ohmic}} \propto i^2$, the overall losses of the FHPWM do not decrease as much for a reduced supply voltage as for the AMSS. At $U_{\text{DC}} = 12.5$ V, both switching strategies have the same power consumption. If the voltage U_{DC} is further decreased, the FHPWM's power consumption exceeds that of the AMSS (see Table II).

The conventional PWM approach shows a similar performance as the FHPWM. Due to the lower switching frequency, the overall losses are slightly lower (see Table II).

VI. NOISE PERFORMANCE INVESTIGATION

A. Theory

Mechanical [31], aerodynamic [32], and electromagnetic sources are distinguished from one another. The contribution of magnetostriction and coil deformation to the electromagnetic noise is very small and can usually be neglected [33]. Beside radial magnetic forces, the torque ripple of electric machines can also be a significant electromagnetic noise source [34]. The resulting noise is the reason why BLDC machines have been rarely used for indoor applications in the past [35]. The torque ripple T_{rip} is the difference of the maximum and the minimum of the instantaneous torque T_{inst}

$$T_{\text{rip}} = \max\left(T_{\text{inst}}\right) - \min\left(T_{\text{inst}}\right). \tag{8}$$

The instantaneous torque is composed of the electro-magnetic torque T_{em} and the cogging torque T_{cog}

$$T_{\text{inst}} = T_{\text{em}} + T_{\text{cog}}. \tag{9}$$

With the single-phase BLDC machines under consideration here, the electro-magnetic torque is derived from the respective phase variables u_{EMF} and i and the mechanical angular velocity

ω_{mech}

$$T_{\text{em}} = \frac{1}{\omega_{\text{mech}}} \left(u_{\text{EMF,A}} \cdot i_{\text{A}} + u_{\text{EMF,B}} \cdot i_{\text{B}}\right) \tag{10}$$

where ω_{mech} is derived from the electrical period, the number of pole pairs p, and the electrical period T_{el} by

$$\omega_{\text{mech}} = \frac{2\pi}{p \cdot T_{\text{el}}}. \tag{11}$$

B. Measurement Setup

All quantities of (10) and (11) were measured with the measurement equipment described in Section V-B.

The cogging torque peaks are very often in the submilli-Newton meter range for FHP permanent magnet (PM) motors and, therefore, challenging to measure. For the example case drive used, the cogging torque was measured with a rheometer [36] with an angular resolution of <10 nrad and a torque resolution of 0.05 nN·m. The maximum deviation of the measured value to the real value of the torque is ±0.5 % with respect to the measured value, but maximum ±0.2 μN·m.

Because international noise standards for automotive auxiliary drives are still under development, the airborne sound measurements were carried out according to the in-house standard VW82469 [37]. To comply with this standard, the measuring microphones have to be placed at a distance of 1 m from the center of the noise source. The orientation of the DUT with respect to the microphones must be selected in such a way that the maximum sound pressure level (SPL) is recorded, and the DUT shall be operated as in the final application.

The structure-borne sound analysis was carried out with three Brüel and Kjaer single-axis acceleration sensors (ISOTRON 2250AM1-1, one for each direction; x, y, and z) mounted on the housings of the fans. The total mass of the sensors should not exceed 10 % of the DUT [38]. A Nexus conditioning amplifier type 2690 was used to process the measurement signals. To obtain the resulting force components, the signals of the three individual directions are added and then multiplied by the mass of the fan system. As with the airborne sound measurements, the fan was suspended with elastomers.

C. Measurement Results

Fig. 5 shows the measured cogging torque, the electromagnetic torque, and the instantaneous torque for the AMSS at the nominal speed of 5000 rpm. Fig. 6 shows the same results for the FHPWM. Independently of the switching strategy, the average value of the instantaneous torque must remain constant to keep the fan at the desired speed ($\overline{T}_{\text{inst}} = 1.54\,\text{mN}\cdot\text{m}$ for $n = 5000\,\text{rpm}$). However, the torque ripple increases from 3.5–7.4 mN·m by the use of the AMSS, compare Figs. 5 and 6. This may increase the emitted airborne and structure-borne sound. This effect is especially pronounced at lower speeds at which the mass moment of inertia cannot smooth the output torque sufficiently.

For frequencies above 400 Hz, the airborne noise is dominated by the broadband in- and outflow noise of the fan [23], thus, it remains almost unaffected by the switching strategy. However, in the frequency range below 400 Hz, the SPLs of the AMSS exceeds the SPLs of the FHPWM, due to the higher torque ripple, see Figs. 7 and 8.

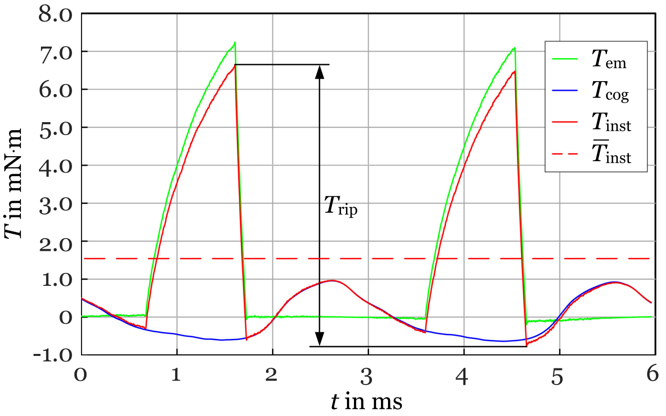

Fig. 5. Measured torques for the AMSS; T_{em} determined as per (10), T_{cog} measured with a rheometer; nominal operating point, $n = 5000$ rpm.

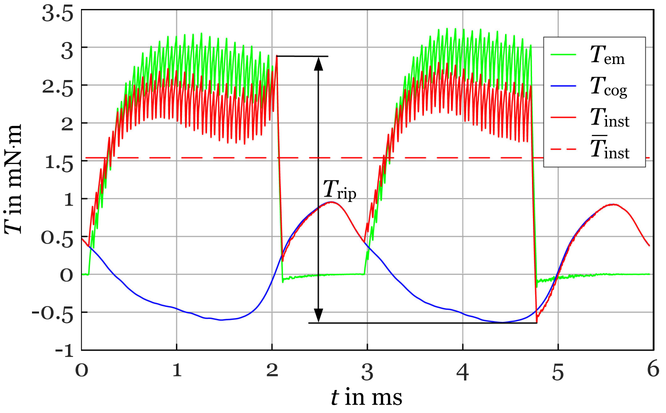

Fig. 6. Measured torques for the FHPWM; T_{em} determined as per (10), T_{cog} measured with a rheometer; nominal operating point, $n = 5000$ rpm.

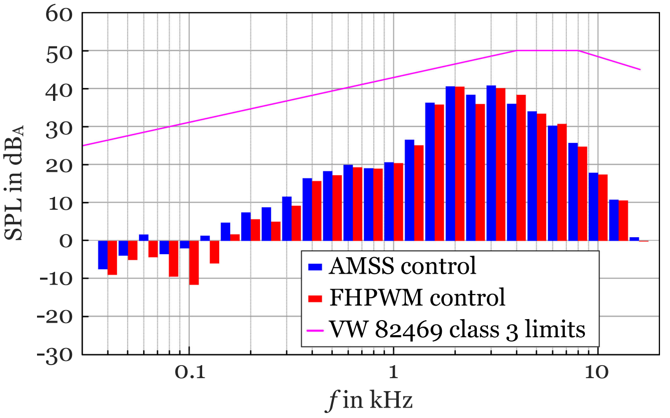

Fig. 7. One-third-octave band analysis of the airborne sound according to [37] for AMSS and FHPWM control, limits VW82469 class 3; nominal operating point, $n = 5000$ rpm.

The increase of the torque ripple can also be seen in Fig. 9. It compares the one-third-octave band analysis of the structure-borne sound for the AMSS and the FHPWM at 5000 rpm. Both switching strategies show a local maxima around 83.3 Hz, which equals the mechanical speed of 5000 rpm.

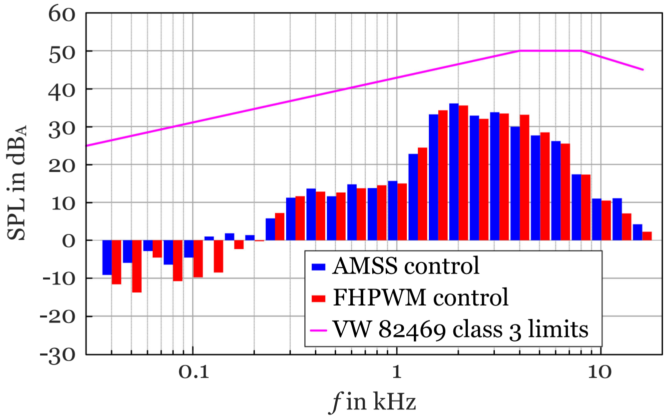

Fig. 8. One-third-octave band analysis of the airborne sound according to [37] for AMSS and FHPWM control, limits VW82469 class 3; $n = 4000$ rpm.

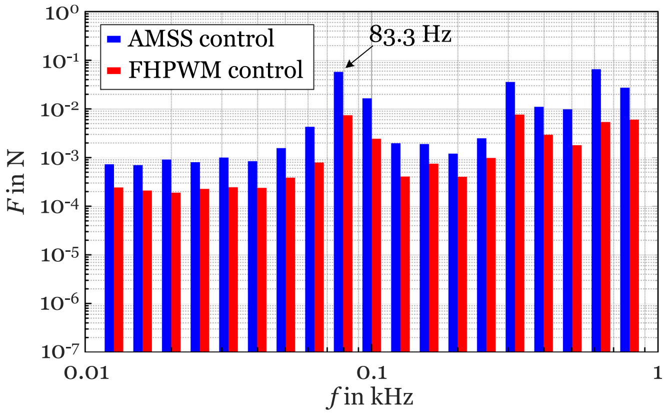

Fig. 9. One-third-octave band analysis of the structure-borne sound for AMSS and FHPWM control; nominal operating point, $n = 5000$ rpm.

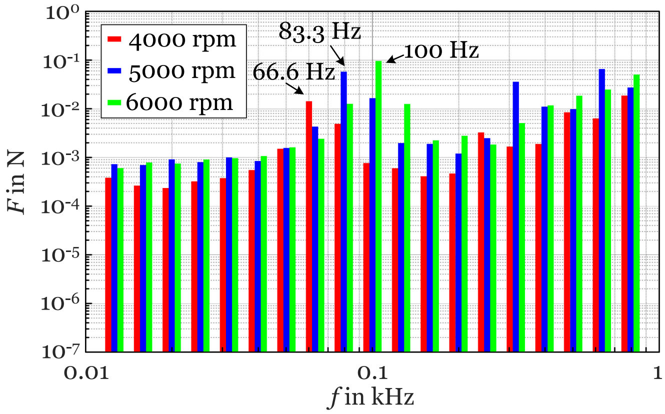

Fig. 10. One-third-octave band analysis of the structure-borne sound for AMSS control, measured at different speeds.

Fig. 10 shows the measured structure-borne sound analysis of the AMSS for 4000, 5000, and 6000 rpm. Because of the distinct peaks of the force at the mechanical speed, the fan operated with the AMSS will more likely stimulate resonances and thus may lead to structure-borne noise problems.

If the supply voltage U_{DC} decreases, also the amplitude of the phase currents of the AMSS decreases. To maintain constant speed, the duration of the phase current blocks must increase accordingly (see Section V). The torque ripple also decreases with the amplitude of the currents [see (8)–(10)]. Thus, while the torque ripple generally increases the structure-born sound at lower frequencies, this noise performance increases if the difference between the supply voltage and the back-EMF decreases.

The airborne and structure-borne sound analyses for the PWM approach is not shown explicitly because they show similar results to the analyses for the FHPWM approach.

TABLE III
PARAMETERS OF THE TWO INVESTIGATED MOTORS

Parameter	Example Case Drive	Higher Power Motor [39]
U_{DC}	8-16 V	13 V
R_{Cu}	8.5 Ω	1.63 Ω
L_{m}	2.8 mH	3.66 mH
τ	329 μs	2.23 ms
n_{nom}	5000 rpm	4100 rpm
T_{nom}	1.54 mN·m	17.3 mN·m
P_{mech}	0.8 W	7.4 W
$\alpha_{\mathrm{prior,n}}$	0°el	57°el
p	2	4

VII. CURRENT AND TORQUE RIPPLE INVESTIGATIONS

This section investigates the influence of the proposed AMSS on the current and torque ripple for motors of different size. In general, the p.u. resistance decreases for motors with increasing output power, for constant supply voltage U_{DC}. The driving voltage for the phase currents is the difference between the supply voltage and the back-EMF, u_{EMF}. Thus, the maximum phase current increases with a decreasing resistance

$$i_{\mathrm{phase}} = f\left(\frac{U_{\mathrm{DC}} - u_{\mathrm{EMF}}}{R}\right). \tag{12}$$

As already stated in Section II, due to the AMSS's low switching frequency, the AMSS does not allow controlling the current amplitude. In contrast, the current will increase with the winding time constant $\tau = {}^{L_{\mathrm{m}}}/_{R_{\mathrm{Cu}}}$ until it reaches its final value, or until the switch is turned OFF again.

As per (8), the torque ripple, T_{rip}, is defined by the difference between the maximum and the minimum of the instantaneous torque. Whereas the instantaneous torque is composed of the electromagnetic torque, T_{em}, and the cogging torque, T_{cog}, see (9), T_{cog} is determined by the motor geometry and the PMs and therefore cannot be influenced during operation. The electromagnetic torque depends on the shape of the current waveform, see (10).

A. *Method of Analysis*

To investigate the influence of the proposed switching strategy on the current and torque ripple for motors of different size, an LTSpice model was implemented. For comparison, a second, higher-power, single-phase BLDC motor with a bifilar winding for an automotive water pump [39] is used. Table III shows its parameters. The output power of the higher power motor is nine times more than that of the example case drive.

TABLE IV
rms AND RIPPLE OF THE PHASE CURRENT FOR THE INVESTIGATED MOTORS OPERATED AT DIFFERENT SPEEDS. PARAMETERS AS PER TABLE III.

Current Comparison									
-	Example Case Drive at 13.5 V			Higher Power Motor at 13 V			Higher Power Motor at 22 V		
$\%n_{\text{nom}}$	I_{rip}	I_{rms}	$I_{\text{rip}}/I_{\text{rms}}$	I_{rip}	I_{rms}	$I_{\text{rip}}/I_{\text{rms}}$	I_{rip}	I_{rms}	$I_{\text{rip}}/I_{\text{rms}}$
%	A	A	-	A	A	-	A	A	-
100	0.846	0.327	2.6	1.85	1.23	1.5	2.3	1.1	2.1
80	0.841	0.233	3.6	1.59	0.791	2.0	2.1	0.808	2.7
60	0.866	0.190	4.6	1.43	0.508	2.8	1.93	0.549	3.5

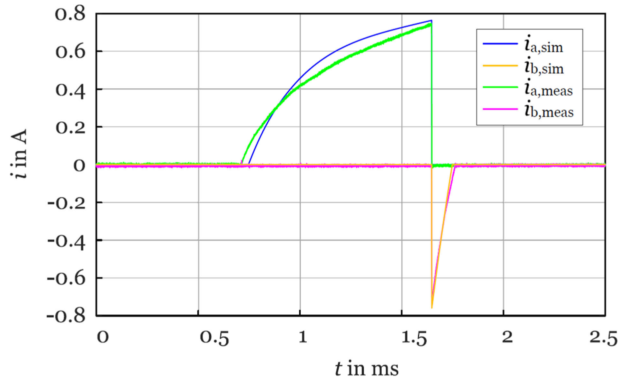

Fig. 11. Model validation: measured and simulated phase currents for the example case drive, AMSS control; nominal operating point, $n = 5000$ rpm.

Inputs for the LTSpice model are the motor parameters R_{Cu}, L_{m}, p, and the wave form of the back-EMF u_{EMF}. [39] does not give any information on the cogging torque of the motor chosen for comparison. Thus, the simulation results for the torque correspond to the electromagnetic torque (10). The load characteristic is modeled with an $M \propto n^2$ characteristic in such a way, that the nominal torque is required at nominal speed. Due to the higher time constant of the higher power motor, the current in one electrical half-period would not rise fast enough to maintain the speed. Therefore, the motor is precommutated with the angle α_{prior}. This angle is adopted linearly with the speed for the simulations for the higher power motor at 13 V.

Fig. 11 shows the simulated and measured phase currents for the example case drive, validating the model.

B. Simulated Current Ripple

1) Nominal Terminal Voltages: Table IV shows the simulated current ripples and rms currents of both investigated BLDC motors for 100%, 80%, and 60% nominal speed, as well as the ratios between the current ripple and the rms-current.

Due to the higher power motor's significantly lower resistance, the time constant increases, (see Table III). Therefore, the time the current needs to reach its final value increases. This in turn reduces the relative current ripple $I_{\text{rip}}/I_{\text{rms}}$ (see Table IV).

2) Elevated Terminal Voltage of the Higher Power Motor: The example case drive is designed for a speed of 5000 rpm at a minimal voltage of 8 V, while the experiments are realized at the nominal voltage of 13.5 V. Due to the higher difference of the back-EMF and the supply voltage, the current ripple is larger than at 8 V operation. To drive the higher power motor in a similar operating point as the example case drive, the supply voltage for the higher power motor was increased to $13\,\text{V}\frac{13.5\,\text{V}}{8\,\text{V}} \approx 22\,\text{V}$. Due to the higher supply voltage, the motor does not need to be precommutated ($\alpha_{\text{prior}} = 0$). The simulation results for the increased voltage are depicted in Table IV.

The influence of the increased supply voltage can be clearly seen by the increased current ripple, the ripple at the nominal speed increases by 24% for the higher power motor (see Table IV).

C. Simulated Torque Ripple

1) Nominal Terminal Voltages: Table V shows the simulated torque ripples and mean values of the electromagnetic torque as per (10) of both investigated BLDC motors for 100%, 80%, and 60% nominal speed. As the high time constant of the higher power motor slows down the current rise and fall times, the higher power motor is energized for a larger share of the electrical half-period to maintain the required speed. Thus, the relative current ripple decreases. This, in turn decreases the relative torque ripple (see Table V).

2) Elevated Terminal Voltage of the Higher Power Motor: Table V shows the simulated torque for the higher power motor at the elevated supply voltage. Here, the elevated voltage leads to a smaller or higher T_{rip}, depending on the precommutation angle α_{prior} of the higher power motor at nominal voltage. For high values of α_{prior}, the positive phase current and the still negative value for the back-EMF results in a small negative peak of the electromagnetic torque. This negative peak has only a small influence on the mean value $\overline{T}_{\text{em}}$. However, it increases the torque ripple T_{rip}, compare to T_{rip} for the higher power motor at 100% nominal speed (see Table V).

D. Results

The current in the phase is determined by the time constant, the ohmic resistance, and the difference between the supply voltage and the back-EMF. If the time constant increases, the current will rise and fall more slowly. Thus, the relative current ripple will decrease. This also positively affects the relative torque ripple.

As the absolute value of the inherent torque ripple of single-phase BLDC motors increases with output power, the sizing

TABLE V
MEAN VALUE AND THE RIPPLE OF THE ELECTROMAGNETIC TORQUE AS PER (10) FOR THE INVESTIGATED MOTORS OPERATED AT DIFFERENT SPEEDS. PARAMETERS AS PER TABLE III.

Torque Comparison									
-	Example Case Drive at 13.5 V			Higher Power Motor at 13 V			Higher Power Motor at 22 V		
$\%n_{\mathrm{nom}}$	T_{rip}	$\overline{T}_{\mathrm{em}}$	$T_{\mathrm{rip}}/\overline{T}_{\mathrm{em}}$	T_{rip}	$\overline{T}_{\mathrm{em}}$	$T_{\mathrm{rip}}/\overline{T}_{\mathrm{em}}$	T_{rip}	$\overline{T}_{\mathrm{em}}$	$T_{\mathrm{rip}}/\overline{T}_{\mathrm{em}}$
%	mN·m	mN·m	-	mN·m	mN·m	-	mN·m	mN·m	-
100	8.1	1.5	5.3	50.6	17.2	3.0	45.9	17.2	2.7
80	8.2	0.82	9.9	41.6	11.0	3.8	50.4	11.1	4.5
60	8.4	0.57	14.8	36.9	6.1	6.0	49.1	6.0	8.1

of single-phase machines is limited [39]. While the AMSS further increases this torque ripple, especially at lower speeds (see Table V) this effect is only minor when compared with the inherent increase due to the motor size.

Thus, the AMSS is a favorable alternative to the PWM approaches to reduce the radiated EME.

VIII. CONCLUSION

This article presents a switching strategy to reduce the radiated EME of FHP drives. The main objective is to reduce the switching frequency down to the electrical frequency of the driven electrical machine, and to adjust the mean value of the voltage by the conduction angle. Thereby, the necessary EMC filter can be reduced. A conventional PWM approach and a frequency hopping PWM approach are used as state-of-the-art references.

Compared with the PWM approaches, the AMSS decreases the radiated EME by almost 10 $\mathrm{dB}_{\mu\mathrm{V/m}}$ over a wide frequency range, although the size of the EMC filter was decreased, down to less than 50%, from nine to four capacitors.

Next, the influence of the new switching approach on the efficiency is investigated. At lower supply voltages, the AMSS performs better than the PWM approaches, whereas the losses within the drive system are higher with higher supply voltages. For the example case drive, the threshold voltage is 12.5 V.

Furthermore, the influence of the proposed AMSS on the airborne and structure-borne sound is investigated. Although the AMSS increases the torque ripple by the increased current amplitudes, the airborne and structure-borne noise does not increase significantly. The structure-borne sound needs to be addressed appropriately by the design of the fan's housing and the suspension thereof. Then, the AMSS allows the EMC filter to be drastically reduced in size, in this case from nine to four capacitors. This also lowers the cost of the electronics and increases its reliability due to the reduced number of components.

Finally, the simulation results of a motor with a more than nine times higher output power than the example case drive are evaluated. Due to the higher time constant of the higher power motor, the relative current and torque ripple decrease, although the absolute values increase. But, this is inherent to single-phase BLDC motors and also limits their size. Thus, the AMSS is a favorable alternative to the PWM approaches to reduce the radiated EME of FHP BLDC motors.

APPENDIX
ADDITIONAL MEASUREMENT RESULTS AT DIFFERENT CONTROL STRATEGIES

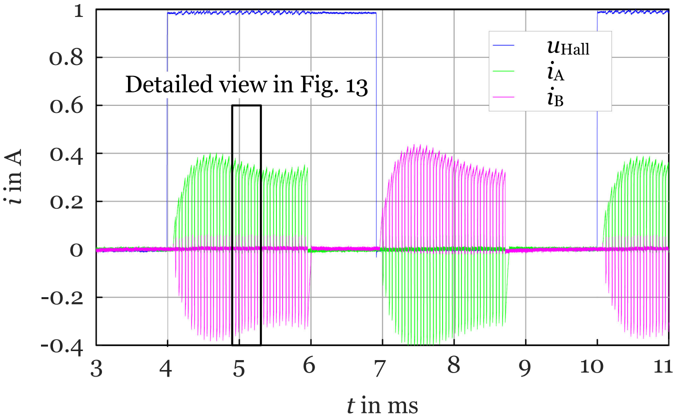

Fig. 12. FHPWM control: measured phase currents and Hall signal; nominal operating point, $n = 5000$ rpm.

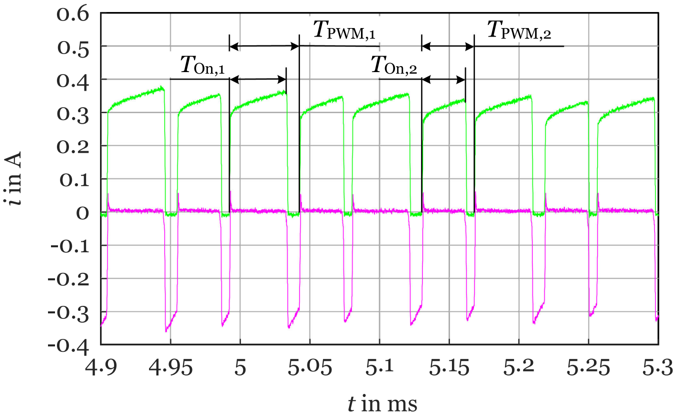

Fig. 13. FHPWM control: measured phase currents, detailed view of 4.9 ms $\leq t \leq$ 5.3 ms; nominal operating point, $n = 5000$ rpm.

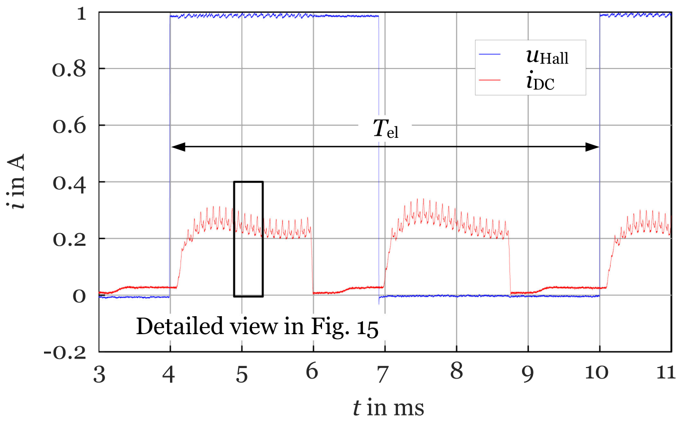

Fig. 14. FHPWM control: measured cable harness current and Hall signal; nominal operating point, $n = 5000$ rpm.

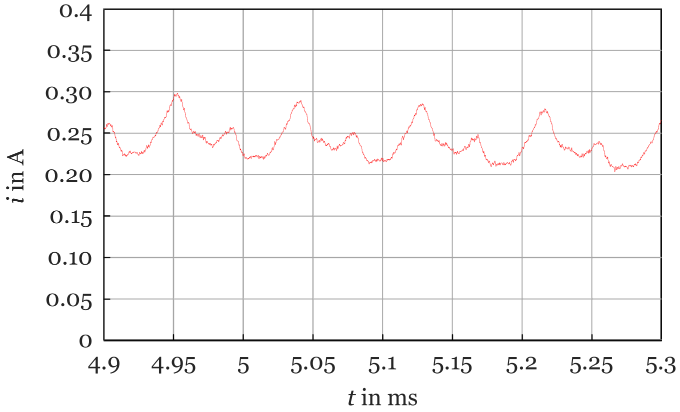

Fig. 15. FHPWM control: measured cable harness current, detailed view of 4.9 ms $\leq t \leq$ 5.3 ms; nominal operating point, $n = 5000$ rpm.

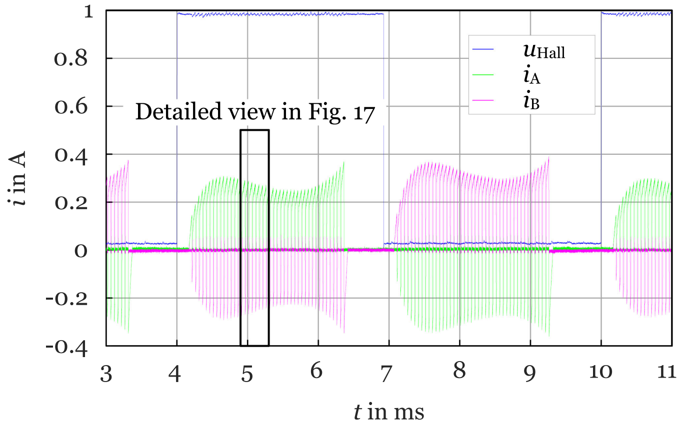

Fig. 16. PWM control: measured phase currents and Hall signal; nominal operating point, $n = 5000$ rpm.

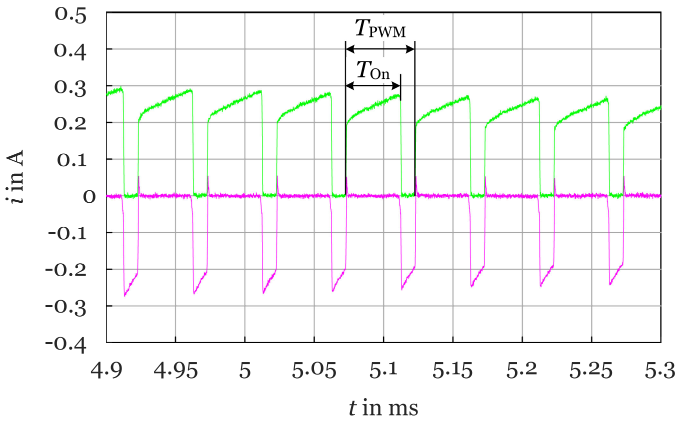

Fig. 17. PWM control: measured phase currents, detailed view of 4.9 ms$\leq t \leq$ 5.3 ms; nominal operating point, $n = 5000$ rpm.

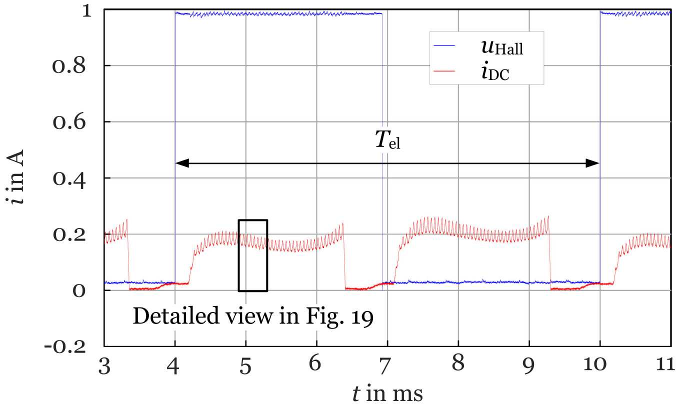

Fig. 18. PWM control: measured cable harness current and Hall signal; nominal operating point, $n = 5000$ rpm.

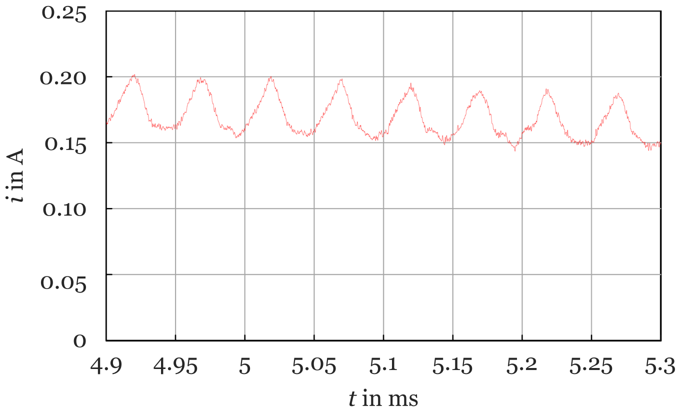

Fig. 19. PWM control: measured cable harness current, detailed view of 4.9 ms$\leq t \leq$ 5.3 ms; nominal operating point, $n = 5000$ rpm.

ACKNOWLEDGMENT

The author would like to thank DI Hans-Joerg Gasser and Dr. Gerhard Schoener from Mechatronic Systems GmbH, Wies, for supplying the prototypes, and Dr. Markus Mosshammer from Mechatronic Systems GmbH, Wies, and DI Stefan Hofmann for their support with the acoustic measurements.

REFERENCES

[1] A. Malvasi, R. Squarcini, G. Armenio, and A. Brömmel, “Design process of an electric powered oil pump,” *MTZ Worldwide*, vol. 73, no. 11, pp. 20–24, 2012. [Online]. Available: https://doi.org/10.1007/s38313-012-0236-0

[2] KSPG Automotive, Ed., *Heartbeat - Das Magazin der KSPG Gruppe*, ser. 02, vol. 2015, Oct. 2015. [Online]. Available: https://www.rheinmetall-automotive.com/unternehmen/informationsmaterial /magazin/

[3] A. Kunz, M. Kunz, H. Vollert, and M. Förster, “Electromechanical brake booster for all drive concepts and automated driving,” *ATZ Worldwide*, vol. 120, no. 4, pp. 58–61, 2018. [Online]. Available: https://doi.org/10.1007/s38311-018-0009-8

[4] S. Rothgang, M. Pachmann, S. Nigrin, and M. von Scheven, “The electric supercharger challenge, conception and implementation,” *MTZ Worldwide*, vol. 76, no. 9, pp. 4–9, 2015. [Online]. Available: https://doi.org/10.1007/s38313-015-0035-5

[5] Volkswagen AG, Wolfsburg, Germany, “erWin Online,” 2019, Accessed: Nov. 19, 2019. [Online]. Available: https://erwin.volkswagen.de/erwin/showHome.do

[6] Volkswagen AG, Wolfsburg, Germany, “Annual Report 2018,” 2019, Accessed: Feb. 19, 2020. [Online]. Available: https://www.volkswagenag.com/en/InvestorRelations/news-and-publications /Annual_Reports.html

[7] J. R. Hendershot and T. J. E. Miller, *Design of Brushless Permanent-Magnet Machines*. Venice, FL, USA: Motor Design Books LLC, 2010.

[8] “CISPR 25:2016 Vehicles, boats and internal combustion engines - Radio disturbance characteristics - Limits and methods of measurement for the protection of on-board receivers,” IEC, CISPR, Oct. 2016.

[9] C. R. Paul, *Introduction to Electromagnetic Compatibility*, 2nd ed. New York, NY, USA: Wiley, 2006.

[10] L. Zhang, H. Ge, Y. Ma, J. Xue, H. Li, and M. Pecht, “Multi-objective optimization design of a notch filter based on improved NSGA-II for conducted emissions,” *IEEE Access*, vol. 8, pp. 83 213–83 223, 2020.

[11] T. Wu, F. Buesink, and F. Canavero, “Overview of signal integrity and EMC design technologies on PCB: Fundamentals and latest progress,” *IEEE Trans. Electromagn. Compat.*, vol. 55, no. 4, pp. 624–638, Aug. 2013.

[12] C. Cuellar and N. Idir, “Stray capacitances determination methods of EMI filter inductors,” in *Proc. 43rd Annu. Conf. IEEE Ind. Electron. Soc.*, 2017, pp. 7040–7045.

[13] S. Marksell, “EMC aspects of PWM controlled loads in vehicles,” Licentiate Thesis, Lund University, Lund, Sweden, 2004.

[14] A. Stone, B. Chambers, and D. Howe, “Random carrier frequency modulation of PWM waveforms to ease EMC problems in switched mode power supplies,” in *Proc. Int. Conf. Power Electron. Drive Syst.*, vol. 1, 1995, pp. 16–21.

[15] J. Balcells, A. Santolaria, A. Orlandi, D. Gonzalez, and J. Gago, “EMI reduction in switched power converters using frequency modulation techniques,” *IEEE Trans. Electromagn. Compat.*, vol. 47, no. 3, pp. 569–576, Aug. 2005.

[16] A. Boudouda, N. Boudjerda, K. E. K. Drissi, and K. Kerroum, “Combined random space vector modulation for a variable speed drive using induction motor,” *Electr. Eng.*, vol. 98, no. 1, pp. 1–15, 2016.

[17] Z. Wang, K. T. Chau, and C. Liu, “Improvement of electromagnetic compatibility of motor drives using chaotic PWM,” *IEEE Trans. Magn.*, vol. 43, no. 6, pp. 2612–2614, Jun. 2007.

[18] F. Pareschi, R. Rovatti, and G. Setti, “EMI reduction via spread spectrum in DC/DC converters: State of the art, optimization, and tradeoffs,” *IEEE Access*, vol. 3, pp. 2857–2874, 2015.

[19] R. Gamoudi, D. Elhak Chariag, and L. Sbita, “A review of spread-spectrum-based PWM techniques’A novel fast digital implementation,” *IEEE Trans. Power Electron.*, vol. 33, no. 12, pp. 10 292–10 307, Dec. 2018.

[20] K. Lee, G. Shen, W. Yao, and Z. Lu, “Performance characterization of random pulse width modulation algorithms in industrial and commercial adjustable-speed drives,” *IEEE Trans. Industry Appl.*, vol. 53, no. 2, pp. 1078–1087, Mar./Apr. 2017.

[21] T. Zeltwanger, H. Sprenger, M. Damson, and M. N. Gupta, “The six-step mode: Unwanted or rather the ideal voltage modulation method,” in *Proc. 19. Internationales Stuttgarter Symposium*, M. Bargende, H.-C. Reuss, A. Wagner, and J. Wiedemann, Eds. Wiesbaden, Germany: Springer Fachmedien Wiesbaden, 2019, pp. 290–304.

[22] I. Ralev, T. Lange, and R. W. De Doncker, “Wide speed range six-step mode operation of IPMSM drives with adjustable dc-link voltage,” in *Proc. 17th Int. Conf. Elect. Mach. Syst.*, 2014, pp. 2987–2993.

[23] P. Zeller, *Handbuch Fahrzeugakustik*, 2nd ed. Berlin, Germany: Vieweg+Teubner Verlag, 2009.

[24] F. Krall, H. Gruebler, and A. Muetze, “Angle modulated switching strategy for fractional horsepower BLDC motors for improved electromagnetic compatibility,” in *Proc. 21st Euro. Conf. Power Electron. Appl.*, Sep. 2019, pp. P.1–P.9.

[25] S. W. Smith, *The Scientist & Engineer’s Guide to Digital Signal Processing*. Pasadena, CA, USA: California Technical Publishing, 1999.

[26] S. Alexandersson, “ Automotive electromagnetic compatibility – Prediction and analysis of parasitic components in conductor layouts,” Ph.D. dissertation, Lund University, Lund, Sweden, 2008.

[27] J. Chen, D. Jiang, and X. Zhao, “A comprehensive investigation on conducted EMI reduction for variable switching frequency PWM,” in *Proc. IEEE Int. Symp. Electromagn. Compat. Asia-Pacific Symp. Electromagn. Compat.*, May 2018, pp. 121–126.

[28] C. Chiu, Y. Chen, Y. Liang, and R. Liang, “Optimal driving efficiency design for the single-phase brushless DC fan motor,” *IEEE Trans. Magn.*, vol. 46, no. 4, pp. 1123–1130, Apr. 2010.

[29] B. Adamczyk, *Foundations of Electromagnetic Compatibility*. Hoboken, NJ, USA: Wiley, 2017.

[30] D. Christen and J. Biela, “Analytical switching loss modeling based on datasheet parameters for MOSFETs in a half-bridge,” *IEEE Trans. Power Electron.*, vol. 34, no. 4, pp. 3700–3710, Apr. 2019.

[31] P. L. Tímár, A. Fazekas, J. Kiss, A. Miklós, and S. J. Yang, *Noise and Vibration of Electrical Machines*. Amsterdam, The Netherlands: Elsevier, 1989.

[32] T. Carolus, *Ventilatoren Aerodynamischer Entwurf, Schallvorhersage, Konstruktion*. Berlin, Germany: Springer Vieweg, 2013.

[33] R. De Doncker, D. U. Sauer, K. Kasper, and M. Bösing, “Vibrationen und Geräusche von elektrischen Antrieben,” Haus der Technik Seminar, Essen, Mar. 2017.

[34] A. A. Mamun, G. Guo, and C. Bi, *Hard Disk Drive Mechantronics and Control*. Boca Raton, FL, USA: CRC Press, 2007.

[35] M. Yoshida, Y. Murai, and M. Takada, “Noise Reduction by Torque Ripple suppression in Brushless DC Motor,” in *Proc. Record. 29th Annual IEEE Power Electron. Specialists Conf.*, vol. 2, May 1998, pp. 1397–1401.

[36] S. Leitner, G. Krenn, H. Gruebler, and A. Muetze, “Rheometer-based cogging and hysteresis torque and iron loss determination of sub-fractional horsepower motors,” *IEEE Trans. Industry Appl.*, vol. 56, no. 4, pp. 3679–3690, Jul./Aug. 2020.

[37] F. Bielert, *Accessory Devices–Acoustic Requirements, Volkswagen Group Standard VW 82469*. Wolfsburg, Germany: Volkswagen AG, Jul. 2014.

[38] “Acoustics determination of airborne sound power levels emitted by machinery using vibration measurement,” ÖNORM, ISO TS 7849, Oct. 2017.

[39] H. Hembach, “Systematischer Vergleich von BLDC-Motorkonzepten mit Anwendung auf nass laufende Wasserpumpen kleiner Leistung,” Ph.D. dissertation, Universität der Bundeswehr München - Fakultät für Elektrotechnik und Informationstechnik, Neubiberg, Germany, 2007.

Felix Krall (Graduate Student Member, IEEE) received the B.Sc. degree and the Dipl.-Ing. degree in electrical engineering in 2015 and 2017, respectively, from the Graz University of Technology, Graz, Austria, where he is currently working toward the Ph.D. degree in electrical engineering with the Electric Drives and Machines Institute.

His research interests include the systems design of fractional hp electric drives and their electromagnetic compatibility.

Mr. Krall is a member of the Christian Doppler Laboratory for Brushless Drives for Pump and Fan Applications.

Hannes Gruebler received the B.Sc. degree and the Dipl.-Ing. degree in electrical engineering in 2012 and 2016, respectively, from the Graz University of Technology, Graz, Austria, where he is currently working toward the Ph.D. degree in electrical engineering with the Electric Drives and Machines Institute.

His research interests include the system-design of small electric drives and their optimization.

Mr. Greubler is a member of the Christian Doppler Laboratory for Brushless Drives for Pump and Fan Applications.

Annette Muetze (Fellow, IEEE) received the Dipl.-Ing. degree in electrical engineering from Darmstadt University of Technology, Darmstadt, Germany, in 1999, the Diploma degree in general engineering from the École Centrale de Lyon, Écully, France, in 1999, and the Dr.-Ing. degree in electrical engineering from Darmstadt University of Technology, in 2004.

She is currently a Full Professor with Graz University of Technology, Graz, Austria, where she heads the Electric Drives and Machines Institute and the Christian Doppler Laboratory for Brushless Drives for Pump and Fan Applications. Prior to joining Graz University of Technology, she was an Assistant Professor with the Department of Electrical and Computer Engineering, University of Wisconsin, Madison, WI, USA, and an Associate Professor with the School of Engineering, University of Warwick, Coventry, U.K.

Prof. Muetze was the recipient of the NSF CAREER Award in 2004.